



MIT Open Access Articles










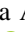


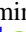





Bright Opportunities for Atmospheric Characterization of Small Planets: Masses and Radii of K2-3 b, c, and d and GJ3470 b from Radial Velocity Measurements and Spitzer Transits

The MIT Faculty has made this article openly available. **Please share** how this access benefits you. Your story matters.

As Published	10.3847/1538-3881/AAF79C
Publisher	American Astronomical Society
Version	Final published version
Citable link	https://hdl.handle.net/1721.1/132393
Terms of Use	Article is made available in accordance with the publisher's policy and may be subject to US copyright law. Please refer to the publisher's site for terms of use.



Bright Opportunities for Atmospheric Characterization of Small Planets: Masses and Radii of K2-3 b, c, and d and GJ3470 b from Radial Velocity Measurements and *Spitzer* Transits

Molly R. Kosiarek^{1,28} , Ian J. M. Crossfield^{1,2}, Kevin K. Hardegree-Ullman³ , John H. Livingston^{4,29} , Björn Benneke⁵, Gregory W. Henry⁶ , Ward S. Howard⁷ , David Berardo² , Sarah Blunt⁸ , Benjamin J. Fulton^{8,30} , Lea A. Hirsch⁹ , Andrew W. Howard⁸ , Howard Isaacson⁹ , Erik A. Petigura^{8,31} , Evan Sinukoff^{10,11} , Lauren Weiss^{12,32} , X. Bonfils¹³, Courtney D. Dressing⁹ , Heather A. Knutson¹⁴, Joshua E. Schlieder¹⁵ , Michael Werner¹⁶, Varoujan Gorjian¹⁶, Jessica Krick¹⁷, Farisa Y. Morales^{18,19,20} , Nicola Astudillo-Defru²¹, J.-M. Almenara²¹, X. Delfosse¹³, T. Forveille¹³, C. Lovis²¹, M. Mayor²¹, F. Murgas^{22,23}, F. Pepe²¹, N. C. Santos^{24,25}, S. Udry²¹, H. T. Corbett⁷, Octavi Fors^{7,26}, Nicholas M. Law⁷ , Jeffrey K. Ratzloff⁷, and Daniel del Ser^{7,27}

¹ Department of Astronomy and Astrophysics, University of California, Santa Cruz, CA 95064, USA; mkosiare@ucsc.edu

² Department of Physics and Kavli Institute for Astrophysics and Space Research, Massachusetts Institute of Technology, Cambridge, MA 02139, USA

³ Department of Physics and Astronomy, The University of Toledo, Toledo, OH 43606, USA

⁴ Department of Astronomy, University of Tokyo, 7-3-1 Hongo, Bunkyo-ku, Tokyo 113-0033, Japan

⁵ Département de Physique, Université de Montréal, 2900 Boulevard Édouard-Montpetit, Montreal, Quebec H3T 1J4, Canada

⁶ Center of Excellence in Information Systems, Tennessee State University, Nashville, TN 37209, USA

⁷ Department of Physics and Astronomy, University of North Carolina at Chapel Hill, Chapel Hill, NC 27599-3255, USA

⁸ California Institute of Technology, Pasadena, CA 91125, USA

⁹ Astronomy Department, University of California, Berkeley, CA 94720, USA

¹⁰ Institute for Astronomy, University of Hawai'i at Mānoa, Honolulu, HI 96822, USA

¹¹ Cahill Center for Astrophysics, California Institute of Technology, 1216 East California Boulevard, Pasadena, CA 91125, USA

¹² University of Montreal, Montreal, QC, H3T 1J4, Canada

¹³ Univ. Grenoble Alpes, CNRS, IPAG, F-38000 Grenoble, France

¹⁴ Division of Geological and Planetary Sciences, California Institute of Technology, Pasadena, CA 91125, USA

¹⁵ Exoplanets and Stellar Astrophysics Laboratory, Code 667, NASA Goddard Space Flight Center, Greenbelt, MD, USA

¹⁶ JPL/Caltech, Pasadena CA 91107, USA

¹⁷ Spitzer Science Center, Caltech, Pasadena CA 91125, USA

¹⁸ Jet Propulsion Laboratory, California Institute of Technology, 4800 Oak Grove Drive, Pasadena, CA 91109, USA

¹⁹ Moorpark College, 7075 Campus Road, Moorpark, CA 93021, USA

²⁰ California State University Northridge, 18111 Nordhoff Street, Northridge, CA 91330, USA

²¹ Observatoire de Genève, Université de Genève, 51 ch. des Maillettes, 1290 Sauverny, Switzerland

²² Instituto de Astrofísica de Canarias (IAC), E-38200 La Laguna, Tenerife, Spain

²³ Dept. Astrofísica, Universidad de La Laguna (ULL), E-38206 La Laguna, Tenerife, Spain

²⁴ Instituto de Astrofísica e Ciências do Espaço, Universidade do Porto, CAUP, Rua das Estrelas, 4150-762 Porto, Portugal

²⁵ Departamento de Física e Astronomia, Faculdade de Ciências, Universidade do Porto, Rua do Campo Alegre, 4169-007 Porto, Portugal

²⁶ Institut de Ciències del Cosmos (ICCUB), Universitat de Barcelona, IEEC-UB, Martí i Franques 1, E-08028 Barcelona, Spain

²⁷ Dept. Física Quàntica i Astrofísica (FQA). Institut de Ciències del Cosmos (ICCUB), Universitat de Barcelona, UB, Martí i Franques 1, E-08028 Barcelona, Spain

Received 2018 March 13; revised 2018 November 21; accepted 2018 December 6; published 2019 February 5

Abstract

We report improved masses, radii, and densities for four planets in two bright M-dwarf systems, K2-3 and GJ3470, derived from a combination of new radial velocity and transit observations. Supplementing *K2* photometry with follow-up *Spitzer* transit observations refined the transit ephemerides of K2-3 b, c, and d by over a factor of 10. We analyze ground-based photometry from the Evryscope and Fairborn Observatory to determine the characteristic stellar activity timescales for our Gaussian Process fit, including the stellar rotation period and activity region decay timescale. The stellar rotation signals for both stars are evident in the radial velocity data and is included in our fit using a Gaussian process trained on the photometry. We find the masses of K2-3 b, K2-3 c, and GJ3470 b to be $6.48_{-0.93}^{+0.99}$, $2.14_{-1.04}^{+1.08}$, and $12.58_{-1.28}^{+1.31} M_{\oplus}$, respectively. K2-3 d was not significantly detected and has a 3σ upper limit of $2.80 M_{\oplus}$. These two systems are training cases for future TESS systems; due to the low planet densities ($\rho < 3.7 \text{ g cm}^{-3}$) and bright host stars ($K < 9 \text{ mag}$), they are among the best candidates for transmission spectroscopy in order to characterize the atmospheric compositions of small planets.

Key words: planets and satellites: composition – techniques: photometric – techniques: radial velocities

Supporting material: machine-readable tables

1. Introduction

The field of exoplanets has shifted from detection to characterization due to technological improvements in instrumentation and large detection surveys such as NASA's *Kepler* mission. One of the most surprising results from *Kepler* was the prevalence of planets between 1 and $4 R_{\oplus}$, called super-Earths

²⁸ NSF Graduate Research Fellow.

²⁹ JSPS Fellow.

³⁰ Texaco Fellow.

³¹ Hubble Fellow.

³² Trotter Fellow.

or sub-Neptunes, which are absent from our solar system (Howard et al. 2012; Dressing & Charbonneau 2013, 2015; Fressin et al. 2013; Petigura et al. 2013). Planets of this size occur more frequently around M stars than G or F stars (Mulders et al. 2015; for orbital periods of <150 days).

Core-accretion models predict that an intermediate sized planet will become the core of a gas giant through runaway gas accretion. Therefore, these models are at odds with the prevalence of such intermediate mass planets (Mizuno 1980; Bodenheimer & Lissauer 2014). To avoid this problem, Lee et al. (2014) and Lee & Chiang (2016) proposed that super-Earths formed later than gas giants, without time to undergo runaway gas accretion. It is also debated whether there is sufficient material in the inner protoplanetary disk to form these planets (Weidenschilling 1977; Hayashi 1981). Pebble accretion and migration could address this problem and form closely packed multiplanet systems orbiting M dwarfs (Swift et al. 2013; Ormel et al. 2017).

Planet compositions provide a crucial link to their formation histories. The composition can be inferred either from the bulk density, which is derived from the planet’s mass and radius, or from atmospheric studies. *Kepler* transits and ground-based radial velocity (RV) follow-up discovered an increase in bulk density with decreasing size, suggesting a transition region at $1.5\text{--}2.0 R_{\oplus}$ between volatile-rich gas/ice planets and rocky planets (Weiss & Marcy 2014; Rogers 2015; Fulton et al. 2017; Van Eylen et al. 2018).

Due to the approaching launch of the *James Webb Space Telescope* (*JWST*) and selection for future the European Space Agency (ESA) mission ARIEL, preparatory measurements of potential atmospheric characterization targets are important for identifying the best targets as well as for the interpretation of the spectra. Primarily, target ephemerides must be refined in order to reduce the transit timing uncertainty and therefore use space-based time most efficiently. Furthermore, precise mass measurements and surface gravity calculations are necessary as these parameters will affect the interpretation of the transmission spectra. Both atmospheric scale height and molecular absorption affect the depth of the planet’s spectroscopic features. Since atmospheric scale height is related to the surface gravity, a precise mass measurement is needed in order to correctly interpret the molecular absorption features in a spectrum (Batalha et al. 2017a).

The *K2* mission has discovered many cool planets orbiting bright stars (Montet et al. 2015; Crossfield et al. 2016; Vanderburg et al. 2016; Dressing et al. 2017; Mayo et al. 2018), and TESS will find a large sample of even brighter systems around nearby stars (Ricker et al. 2014; Sullivan et al. 2015). These bright host stars can be more precisely followed up from ground-based telescopes and are amenable to transmission spectroscopy observations. This paper illustrates a follow-up program to prepare for potential *JWST* observations of two systems much like those that will be found by TESS.

In this paper we describe precise RV and photometry follow-up of two systems, K2-3 and GJ3470. Both of these systems have sub-Neptune-sized planets orbiting M-dwarf stars and are amenable to atmospheric transmission spectroscopy. In Section 2 we describe the two systems. In Section 3 we detail our *Spitzer* observations and analysis. In Section 4 we describe our RV analysis and related photometric follow-up, then present our RV results. In Section 5 we examine these planets in the context of other similar sub-Neptune systems and discuss

Table 1
K2-3 Stellar Properties

Parameter	Value	Units	Source
<i>Identifying Information</i>			
R.A.	11:29:20.388		(1)
Decl.	−01:27:17.23		(1)
<i>Photometric Properties</i>			
<i>J</i>	9.421 ± 0.027	mag	(2)
<i>H</i>	8.805 ± 0.044	mag	(2)
<i>K</i>	8.561 ± 0.023	mag	(2)
<i>Kp</i>	11.574	mag	(3)
Rotation Period	40 ± 2	days	(4)
<i>Spectroscopic Properties</i>			
Barycentric RV	32.6 ± 1	km s^{-1}	(1)
Distance	45 ± 3	pc	(1)
H α	0.38 ± 0.06	Ang	(1)
Age	≥ 1	Gyr	(1)
Spectral Type	M0.0 \pm 0.5 V		(1)
[Fe/H]	-0.32 ± 0.13		(1)
Temperature	3896 ± 189	K	(1)
Mass	0.601 ± 0.089	M_{\odot}	(1)
Radius	0.561 ± 0.068	R_{Sun}	(1)
Density	3.58 ± 0.61	ρ_{Sun}	(5)
Surface Gravity	4.734 ± 0.062	cgs	(5)

Note. (1) Crossfield et al. (2015), (2) Cutri et al. (2003), (3) Huber et al. (2016), (4) this work, (5) Almenara et al. (2015).

atmospheric transmission spectroscopy considerations before concluding in Section 6.

2. Target Systems and Stellar Parameters

K2-3 (EPIC 201367065) is a bright ($K_s = 8.6$ mag), nearby (45 ± 3 pc) M0 dwarf star hosting three planets from 1.5 to $2 R_{\oplus}$ at orbital periods between 10 and 45 days (Crossfield et al. 2015; Table 1). These planets receive 1.5–10 times the flux incident on Earth and planet d orbits near the habitable zone.

K2-3 b, c, and d were discovered in *K2* photometry (Crossfield et al. 2015). Since then, there have been multiple RV and transit follow-up measurements. Almenara et al. (2015) collected 66 HARPS spectra and determined the masses of planet b, c, and d to be 8.4 ± 2.1 , $2.1^{+2.1}_{-1.3}$, and $11.1 \pm 3.5 M_{\oplus}$, respectively. Almenara et al. (2015) caution that the RV semi-amplitudes of planets c and d are likely affected by stellar activity. Dai et al. (2016) collected 31 spectra with the Planet Finder Spectrograph (PFS) on *Magellan* and modeled the RV data with Almenara’s HARPS data. The combined data sets constrained the masses of planets b, c, and d to be 7.7 ± 2.0 , <12.6 , and $11.3^{+5.9}_{-3.8} M_{\oplus}$, respectively. Damasso et al. (2018) performed an RV analysis on a total of 132 HARPS spectra and 197 HARPS-N spectra, including the Almenara sample. This HARPS analysis found the mass of planet b and c to be 6.6 ± 1.1 and $3.1^{+1.3}_{-1.2} M_{\oplus}$, respectively. The mass of planet d is estimated as $2.7^{+1.2}_{-0.8}$ from a suite of injection-recovery tests. Beichman et al. (2016) refined the ephemeris and radii of the three planets with seven follow-up *Spitzer* transits and Fukui et al. (2016) observed a ground-based transit of K2-3 d to further refine its ephemeris.

GJ3470 is also a bright ($K = 8.0$ mag), nearby ($29.9^{+3.7}_{-3.4}$ pc) M1.5 dwarf hosting one Neptune-sized planet in a 3.33 day orbit (Cutri et al. 2003; Bonfils et al. 2012; Table 2). GJ3470 b

Table 2
GJ3470 Stellar and Planet b Transit Properties

Parameter	Value	Units	Source
<i>Photometric Properties</i>			
Spectral Type	M1.5		(1)
V	12.3	mag	(2)
K	7.989 ± 0.023	mag	(3)
J	8.794 ± 0.019	mag	(3)
H	8.206 ± 0.023	mag	(3)
Rotation Period	21.54 ± 0.49	days	(5)
<i>Spectroscopic Properties</i>			
Luminosity	0.029 ± 0.002	L_{\odot}	(2)
Mass	0.51 ± 0.06	M_{\odot}	(4)
Radius	0.48 ± 0.04	R_{\odot}	(4)
Distance	$30.7^{+2.1}_{-1.7}$	pc	(6)
Age	0.3–3	Gyr	(2)
Temperature	3652 ± 50	K	(4)
Surface Gravity	4.658 ± 0.035	cgs	(6)
[Fe/H]	$+0.20 \pm 0.10$		(6)
<i>Transit Properties</i>			
T_0 (–2450,000)	6677.727712 ± 0.00022	BJD	(7)
T_{14}	$0.07992^{+0.00100}_{-0.00099}$	days	(7)
P	3.3366413 ± 0.0000060	days	(7)
R_p	3.88 ± 0.32	R_{\oplus}	(4)
a/R_*	$12.92^{+0.72}_{-0.65}$		(7)
T_{eq}	615 ± 16	K	(2)

Note. (1) Reid et al. (1997), (2) Bonfils et al. (2012), (3) Cutri et al. (2003), (4) Biddle et al. (2014), (5) this work, (6) Demory et al. (2013), (7) Dragomir et al. (2015).

was discovered in a HARPS RV campaign that searched for short-period planets orbiting M dwarfs and was subsequently observed in transit. GJ3470 b has an equilibrium temperature near 700 K and a radius of $3.9 R_{\oplus}$. Its mass has been measured previously to be 13.73 ± 1.61 , 14.0 ± 1.8 , and $13.9^{+1.5}_{-1.4} M_{\oplus}$ by Bonfils et al. (2012), Demory et al. (2013), and Biddle et al. (2014), respectively. Its low density supports a substantial atmosphere covering the planet (Biddle et al. 2014). Seven previous studies have investigated its atmospheric composition. Fukui et al. (2013) found variations in the transit depths in the J , I , and $4.5 \mu\text{m}$ bands that suggest that the atmospheric opacity varies with wavelength due to the absorption or scattering of stellar light by atmospheric molecules. Nascimbeni et al. (2013) detected a transit depth difference between the ultraviolet and optical wavelengths also indicating a Rayleigh-scattering slope, confirmed by Biddle et al. (2014), Dragomir et al. (2015), and Chen et al. (2017). Crossfield et al. (2013) found a flat transmission spectrum in the K -band suggesting a hazy, methane-poor, or high-metallicity atmosphere. Finally, Bourrier et al. (2018) finds the planet is surrounded by a large exosphere of neutral hydrogen from Hubble Lyman alpha measurements.

3. K2-3 *Spitzer* Observations

We observed six transits of K2-3 b, two transits of K2-3 c, and two transits of K2-3 d using Channel 2 ($4.5 \mu\text{m}$) of the Infrared Array Camera (IRAC) on the *Spitzer Space Telescope* to refine the transit parameters of these three planets (GO 11026, PI: Werner; GO 12081, PI: Benneke). K2-3 was observed in staring mode and placed on the “sweet spot” pixel to keep the star in one location during the observations and minimize the effect of gain variations. To minimize data volume and overhead from readout time, the subarray mode was used with an exposure time

of 2 s per frame. This produced between 11392 and 26368 individual frames per observation. Total observation durations were between 6.5 and 15 hr to include the adequate out-of-transit baseline and were typically centered near the predicted mid-transit time from the *K2* ephemeris.

In the following subsection, we describe two different analyses performed on these *Spitzer* data. The first analysis performs an individual fit to each *Spitzer* transit separately to check for consistency of the parameters between individual transit events whereas the second analysis performs a combined fit to the *Spitzer* data to derive global parameters.

3.1. *Spitzer* Transit Analysis

We extract the *Spitzer* light curves following the approach taken by Knutson et al. (2012) and Beichman et al. (2016), using a circular aperture 2.4 pixels in radius centered on the host star. We used the Python package *photutils* (Bradley et al. 2016) for centroiding and aperture photometry. We use a modified version of the pixel-level decorrelation (PLD; Deming et al. 2015) adapted from Benneke et al. (2017) to simultaneously model the *Spitzer* systematics (intra-pixel sensitivity variations) and the exoplanet system parameters. The instrument sensitivity is modeled by Equation (1) in Benneke et al. (2017), and we use the Python package *batman* (Kreidberg 2015) to generate the transit models. For parameter estimation we use the Python package *emcee* (Foreman-Mackey et al. 2013), an implementation of the affine-invariant Markov chain Monte Carlo (MCMC) ensemble sampler (Goodman & Weare 2010). We find that using a 3×3 pixel grid sufficiently captures the information content corresponding to the motion of the point-spread function (PSF) on the detector (which is typically \lesssim a few tenths of a pixel). In comparisons between various methods used to correct *Spitzer* systematics (Ingalls et al. 2016), PLD was among the top performers, displaying both high precision and repeatability. For more details about this type of IRAC photometry analysis, see Livingston et al. (2019) and K. Hardegree-Ullman (2019, in preparation).

We first analyzed the *Spitzer* transits one at a time to check for consistency of parameters between independent transit events. For the individual transit models, we fit for the scaled planet radius R_p/R_* , the mid-transit time T_0 , the scaled semimajor axis a/R_* , and the orbital inclination angle i . The quadratic limb-darkening coefficients for the $4.5 \mu\text{m}$ *Spitzer* bandpass were found by interpolating the values from Claret & Bloemen (2011). We held the orbital periods constant at the values found by Beichman et al. (2016), and fixed eccentricity and longitude of periastron to 0, but note that these parameters have a negligible effect on the overall shape of the transit model. Gaussian priors were imposed on the transit system parameters based on our previous knowledge of the system from Crossfield et al. (2015). We also found global system parameters by combining the posterior distributions from each individual result for each planet and finding the 16th, 50th, and 84th percentiles of the combined distribution. One example transit is shown in Figure 1.

We then perform our global fit to the 10 *Spitzer* transit data sets of the three planets in this system by constructing a joint model comprising a set of shared transit parameters and a set of systematic parameters corresponding to each individual transit observation. We adopt a global quadratic limb-darkening law and set Gaussian priors on the parameters u_1 and u_2 by interpolating the table of Claret et al. (2012), where the widths are determined by a Monte Carlo simulation. To restrict

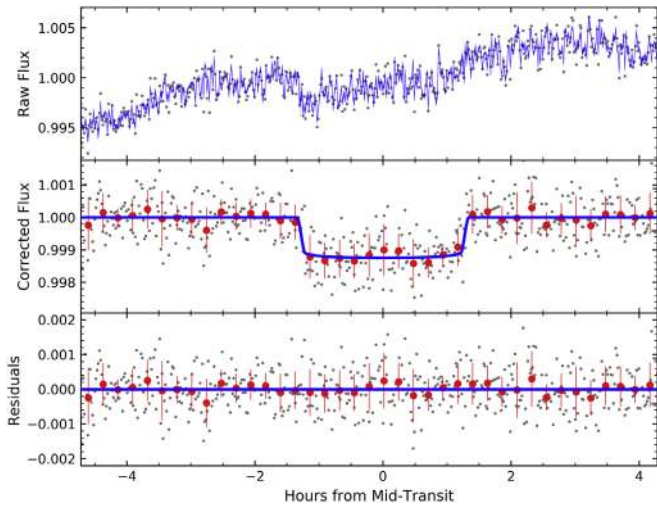


Figure 1. Example fit to one transit of K2-3 b. Top: raw *Spitzer* data (black points) including the fit to the systematics (blue line). Middle: transit of K2-3 b including raw data (gray points), binned data (red points), and transit model (blue line). Bottom: residuals from the model.

exploration of limb-darkening parameter space to only physical scenarios, we utilize the triangular sampling method of Kipping (2013); thus, we actually sample in the q_1/q_2 space. For each of the three planets in the system, we use a unique set of transit parameters: the period P , time of mid-transit T_0 , planet-star radius ratio R_p/R_* , scaled semimajor axis a/R_* , and impact parameter b . The rest of the parameters in the model correspond to the PLD coefficients for each individual data set. Besides the Gaussian priors on the limb-darkening parameters, we also impose Gaussian priors on T_0 , P , and the mean stellar density of the host star, based on the values reported in Crossfield et al. (2015). See Figure 2 for the transit fits for K2-3 b, c, and d obtained from our global *Spitzer* analysis.

All of our transit parameters are shown in Table 3 along with the parameters derived from only the K2 transits for comparison (Crossfield et al. 2015). We combined the parameters from the individual fits by adding their posteriors in order to compare the individual fits with the global analysis. The parameters from these two analyses are all within 1σ . We adopt the parameters from the simultaneous transit analysis for our RV analysis.

3.2. *Spitzer* Ephemeris Improvement

These *Spitzer* data reduce the uncertainty on the transit times and periods of the K2-3 planets. Refining the ephemerides is particularly important in order to efficiently subdivide time on large telescopes and space-based telescopes. Figure 3 shows the uncertainty of the transit time of each planet propagated forwards to 2022, shortly after the launch of *JWST*. This refinement is crucial to accurately schedule transit observations with future space-based atmospheric missions. For example, if one wanted to observe K2-3 d in the *JWST* era, the K2 3σ uncertainty of the transit mid-point is over 25 hr; this would waste considerable telescope time and will only increase as the time baseline lengthens. Beichman et al. (2016) refined its ephemeris with *Spitzer* measurements two years ago. Our measurements further refine the orbital period uncertainty by a over factor of twenty from the original K2 data and to one-third of that from Beichman et al. (2016). From our *Spitzer* analysis,

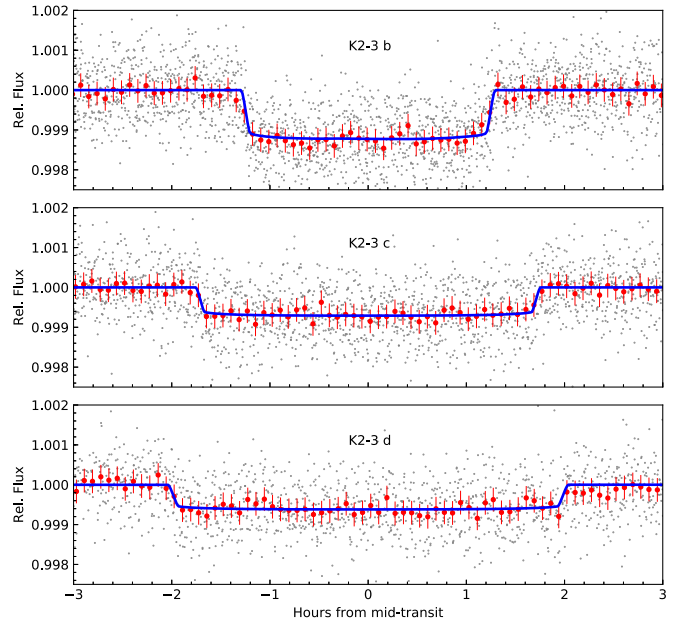


Figure 2. Transit fits to K2-3 b, c, and d displaying all of our *Spitzer* data for each planet. Individual *Spitzer* data points (gray), binned points (red), and planet fits from our simultaneous analysis (blue) for each K2-3 planet are shown.

the 3σ uncertainty in the transit mid-point of K2-3 d in 2022 has improved to only 30 minutes.

4. RV Analysis

4.1. RV Observations

We obtained RV measurements of K2-3 and GJ3470 using the High Resolution Echelle Spectrometer (HIRES; Vogt et al. 1994) on the Keck I Telescope. We collected 74 measurements of K2-3 from 2015 February 4 to 2017 April 11 and 56 measurements of GJ3470 from 2012 September 25 to 2017 March 15. These spectra were taken with an iodine cell and the C2 decker; a template spectrum was also taken in order to calibrate the wavelength and estimate the RV uncertainty. On average, measurements of K2-3 were collected with an exposure time of 1600 s in order to reach a signal-to-noise (S/N) ratio of 87/pixel (80k counts on the HIRES exposure meter). Measurements of GJ3470 were collected with an exposure time of 1200 s in order to reach an S/N of 60/pixel (40k counts). The observations and data reduction followed the California Planet Search method described in Howard et al. (2010). RV data for K2-3 and GJ3470 are shown in Tables 4 and 5.

An additional 360 Doppler measurements were used in the following K2-3 analysis. We include 31 spectra collected with PFS (Dai et al. 2016), 132 spectra collected with HARPS, and 197 spectra collected with HARPS-N (Almenara et al. 2015; Damasso et al. 2018). Our HIRES measurements have an average uncertainty of 1.7 m s^{-1} , whereas the PFS, HARPS, and HARPS-N measurements have average uncertainties of 2.5 m s^{-1} , 2.1 m s^{-1} , and 2.0 m s^{-1} , respectively. An additional 114 Doppler measurements collected with HARPS were used in the following GJ3470 analysis, 61 from the original discovery paper (Bonfils et al. 2012) and 53 additional measurements taken in the same fashion (Astudillo-Defru et al. 2015, 2017). Our HIRES measurements have an average

Table 3
K2-3 *Spitzer* Transit Fit Parameters

Planet	P (days)	Mid-transit (BJD)	R_p/R_* (%)	R_p/R_{\oplus}	a/R_*	i ($^{\circ}$)	b	Source
b	...	2457094.94680 ^{+0.00080} _{-0.00068}	3.494 ^{+0.087} _{-0.087}	2.134 ^{+0.272} _{-0.260}	29.44 ^{+3.89} _{-3.91}	89.50 ^{+0.35} _{-0.43}	0.26 ^{+0.21} _{-0.17}	IRAC2 Transit 1
b	...	2457105.00241 ^{+0.00068} _{-0.00062}	3.864 ^{+0.094} _{-0.095}	2.366 ^{+0.298} _{-0.300}	29.478 ^{+3.93} _{-3.88}	89.56 ^{+0.30} _{-0.39}	0.23 ^{+0.19} _{-0.16}	IRAC2 Transit 2
b	...	2457275.92778 ^{+0.00149} _{-0.00121}	3.355 ^{+0.090} _{-0.090}	2.053 ^{+0.259} _{-0.258}	29.54 ^{+3.91} _{-3.99}	89.31 ^{+0.45} _{-0.50}	0.35 ^{+0.25} _{-0.23}	IRAC2 Transit 3
b	...	2457466.97119 ^{+0.00114} _{-0.00086}	3.360 ^{+0.084} _{-0.085}	2.057 ^{+0.253} _{-0.260}	29.43 ^{+3.89} _{-3.95}	89.46 ^{+0.37} _{-0.46}	0.27 ^{+0.23} _{-0.18}	IRAC2 Transit 4
b	...	2457497.13286 ^{+0.00107} _{-0.00111}	3.659 ^{+0.088} _{-0.088}	2.237 ^{+0.286} _{-0.271}	29.52 ^{+4.02} _{-4.00}	89.42 ^{+0.40} _{-0.49}	0.30 ^{+0.24} _{-0.20}	IRAC2 Transit 5
b	...	2457627.84302 ^{+0.00090} _{-0.00232}	3.572 ^{+0.090} _{-0.091}	2.192 ^{+0.267} _{-0.266}	29.46 ^{+3.89} _{-3.92}	89.52 ^{+0.33} _{-0.44}	0.25 ^{+0.21} _{-0.17}	IRAC2 Transit 6
b	10.054638 ± 0.000016	...	3.532 ^{+0.243} _{-0.185}	2.165 ^{+0.297} _{-0.284}	29.43 ^{+3.93} _{-3.91}	89.47 ^{+0.37} _{-0.46}	0.27 ^{+0.22} _{-0.19}	Individual Combined
b	10.054626 ^{+0.000099} _{-0.000010}	2456813.41843 ^{+0.00039} _{-0.00038}	3.44 ^{+0.04} _{-0.04}	2.103 ^{+0.257} _{-0.256}	30.02 ^{+0.25} _{-0.31}	89.588 ^{+0.116} _{-0.100}	0.22 ^{+0.05} _{-0.06}	Simultaneous Fit
b	10.05403 ^{+0.00026} _{-0.00025}	2456813 ± 0.0011	3.483 ^{+0.123} _{-0.070}	2.14 ^{+0.27} _{-0.26}	29.2 ^{+1.8} _{-3.6}	89.28 ^{+0.46} _{-0.60}	0.37 ^{+0.22} _{-0.23}	Crossfield et al. (2015)
c	...	2457108.03664 ^{+0.00172} _{-0.00187}	2.549 ^{+0.080} _{-0.081}	1.557 ^{+0.197} _{-0.190}	53.62 ^{+7.12} _{-7.13}	89.73 ^{+0.21} _{-0.27}	0.29 ^{+0.24} _{-0.19}	IRAC2 Transit 1
c	...	2457280.56131 ^{+0.00215} _{-0.00224}	2.554 ^{+0.080} _{-0.081}	1.559 ^{+0.198} _{-0.195}	53.28 ^{+7.19} _{-7.23}	89.69 ^{+0.21} _{-0.27}	0.28 ^{+0.24} _{-0.20}	IRAC2 Transit 2
c	...	2457477.73145 ^{+0.00254} _{-0.00253}	2.670 ^{+0.081} _{-0.081}	1.635 ^{+0.204} _{-0.200}	53.30 ^{+7.15} _{-7.07}	89.72 ^{+0.19} _{-0.26}	0.26 ^{+0.24} _{-0.18}	IRAC2 Transit 3
c	...	2457625.61918 ^{+0.00171} _{-0.00199}	2.726 ^{+0.077} _{-0.081}	1.668 ^{+0.211} _{-0.207}	53.49 ^{+7.10} _{-7.03}	89.73 ^{+0.19} _{-0.25}	0.26 ^{+0.22} _{-0.19}	IRAC2 Transit 4
c	...	2457650.26528 ^{+0.00191} _{-0.00129}	2.743 ^{+0.079} _{-0.079}	1.680 ^{+0.209} _{-0.207}	53.67 ^{+7.00} _{-7.01}	89.72 ^{+0.19} _{-0.24}	0.26 ^{+0.22} _{-0.18}	IRAC2 Transit 5
c	24.646569 ± 0.000047	...	2.653 ^{+0.116} _{-0.128}	1.618 ^{+0.212} _{-0.207}	53.47 ^{+7.10} _{-7.15}	89.71 ^{+0.20} _{-0.26}	0.27 ^{+0.23} _{-0.19}	Individual Combined
c	24.646582 ^{+0.000039} _{-0.000039}	2456812.28013 ^{+0.00090} _{-0.00095}	2.59 ^{+0.06} _{-0.06}	1.584 ^{+0.197} _{-0.195}	54.57 ^{+0.46} _{-0.56}	89.905 ^{+0.066} _{-0.088}	0.09 ^{+0.08} _{-0.06}	Simultaneous Fit
c	24.6454 ± 0.0013	2456812 ^{+0.00026} _{-0.00025}	2.786 ^{+0.143} _{-0.083}	1.72 ^{+0.23} _{-0.22}	51.8 ^{+4.1} _{-9.1}	89.55 ^{+0.29} _{-0.44}	0.41 ^{+0.26} _{-0.25}	Crossfield et al. (2015)
d	...	2457093.56831 ^{+0.00517} _{-0.00325}	2.479 ^{+0.089} _{-0.089}	1.521 ^{+0.191} _{-0.190}	79.09 ^{+10.55} _{-10.73}	89.81 ^{+0.13} _{-0.17}	0.27 ^{+0.23} _{-0.19}	IRAC2 Transit 1
d	...	2457271.79827 ^{+0.00477} _{-0.00359}	2.490 ^{+0.088} _{-0.089}	1.521 ^{+0.194} _{-0.191}	79.74 ^{+10.63} _{-10.82}	89.81 ^{+0.13} _{-0.17}	0.27 ^{+0.23} _{-0.19}	IRAC2 Transit 2
d	...	2457494.57861 ^{+0.00405} _{-0.00296}	2.454 ^{+0.082} _{-0.083}	1.503 ^{+0.184} _{-0.191}	79.51 ^{+10.55} _{-10.67}	89.79 ^{+0.14} _{-0.17}	0.30 ^{+0.22} _{-0.20}	IRAC2 Transit 3
d	...	2457628.23815 ^{+0.00891} _{-0.00200}	2.449 ^{+0.081} _{-0.082}	1.500 ^{+0.189} _{-0.185}	79.69 ^{+10.78} _{-10.63}	89.80 ^{+0.14} _{-0.17}	0.29 ^{+0.24} _{-0.20}	IRAC2 Transit 4
d	44.556913 ± 0.000182	...	2.468 ^{+0.086} _{-0.087}	1.511 ^{+0.191} _{-0.193}	79.35 ^{+10.71} _{-10.53}	89.80 ^{+0.14} _{-0.17}	0.28 ^{+0.23} _{-0.19}	Individual Combined
d	44.556456 ^{+0.000097} _{-0.000087}	2456826.22347 ^{+0.00053} _{-0.00052}	2.44 ^{+0.08} _{-0.08}	1.492 ^{+0.189} _{-0.186}	80.98 ^{+0.68} _{-0.84}	89.788 ^{+0.033} _{-0.029}	0.30 ^{+0.04} _{-0.05}	Simultaneous Fit
d	44.5631 ^{+0.0063} _{-0.0043}	2456826 ^{+0.00037} _{-0.00043}	2.48 ^{+0.14} _{-0.10}	1.52 ^{+0.21} _{-0.20}	78.7 ^{+6.7} ₋₁₃	89.68 ^{+0.21} _{-0.26}	0.45 ^{+0.23} _{-0.28}	Crossfield et al. (2015)

uncertainty of 1.9 m s^{-1} while the two sets of HARPS measurements have an average uncertainty of 4.2 m s^{-1} .

4.2. Stellar Activity

Magnetic activity on the stellar surface can induce planet-like signals in RV data (Robertson et al. 2013, 2015). This is especially problematic for M dwarfs, where the magnetic activity is not as well characterized as for solar-type stars and the stellar rotation period is often similar to planet orbital periods at days to tens of days (McQuillan et al. 2013; Newton et al. 2016). The stellar activity also causes absorption line variability (Cincunegui et al. 2007; Buccino et al. 2011; Gomes da Silva et al. 2012), which can be tracked by measuring tracers such as the Calcium II H and K lines noted as S_{HK} . S_{HK} measurements may not always indicate activity for M dwarfs (Robertson et al. 2015); both photometry and H α can be useful diagnostics for M-dwarf stellar rotation periods (Newton et al. 2017).

We first examined the potential effects of stellar activity by measuring the strength of these Calcium II H and K spectral lines in our HIRES RV measurements (Isaacson & Fischer 2010). We calculated the correlation coefficient and probability value (p -value) for the S_{HK} and RV data for each season of data collection (using `scipy`; Jones et al. 2001). Then, we examined the RV and S_{HK} periodograms for potential similarities. We also analyzed ground-based photometry of K2-3 and GJ3470 to determine the rotation period and compared this period to the RV periodograms. Finally, we modeled the RV data of K2-3 and GJ3470 with Gaussian processes (GPs) trained on the photometry to remove correlated noise in the RVs from the stellar activity.

4.2.1. K2-3 Stellar Activity and Ground-based Photometry

We investigate the possible correlation between S_{HK} and RV values for K2-3 (Table 4) as the stellar rotation period found from K2 photometry (40 ± 10 days; Dai et al. 2016) is near the orbital period of planet d. Dai et al. (2016) and Damasso et al. (2018) find the planet signal to be degenerate with the stellar rotation signal. The correlation coefficient is -0.0169 and p -value is 0.8869 for the full data set, suggesting that the RVs are not correlated with the stellar activity as measured by S_{HK} . We also do not find any similar significant peaks in the periodograms (Figure 4). However, as the RV periodogram does not show all of the planet signals, the activity signals may also be hidden.

As mentioned above, S_{HK} may be a poor indicator for M-dwarf stars. To better characterize the possible rotation signal of K2-3, we analyzed photometry from the Evryscope. The Evryscope is an array of 24 61 mm telescopes together imaging 8000 square degrees of sky every 2 minutes (Law et al. 2015). Since its 2015 installation at Cerro Tololo Inter-American Observatory (CTIO) in Chile, the Evryscope has observed on over 500 clear nights, tracking the sky for 2 hr at a time before ratcheting back and continuing observations, for an average of ~ 6 hr of continuous monitoring each night. The Evryscope observes in Sloan- g' at a resolution of $13''/\text{pixel}$. High-cadence photometry of K2-3 is included in the Evryscope light curve database from 2016 January to 2018 March (Figure 5). Because K2-3 is in the northernmost region of the Evryscope field of view, the coverage of the target is limited each year, resulting in a total of 10^4 epochs; most southern stars are observed with $4\text{--}6\times$ more points.

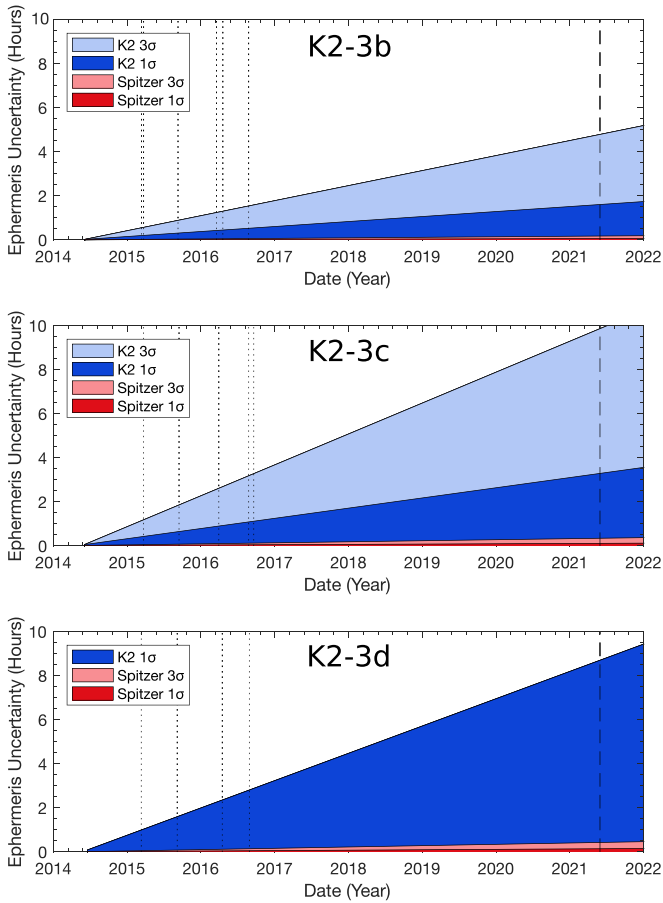


Figure 3. Transit time uncertainty for the K2-3 system in the *JWST* era. The blue region illustrates the 3σ uncertainty (light blue) and 1σ uncertainty (dark blue) on the transit times from the K2-derived ephemerides reported by Crossfield et al. (2015). Equivalently, the red region illustrates the 1σ and 3σ uncertainty on the transit times from our *Spitzer*-derived ephemerides. The vertical dotted lines illustrate the times of the *Spitzer* observations. The vertical dashed line shows the scheduled *JWST* launch in 2021 March. The *Spitzer* transits decrease the uncertainty on the transit times by over a factor of 10.

Table 4
K2-3 HIRES Relative RV Measurements

BJD _{TDB}	RV (m s ⁻¹)	Unc. (m s ⁻¹)	$S_{HK} \pm 0.005$
2457057.93921	0.36	2.33	0.9000
2457058.03821	-0.95	1.73	0.7805
2457058.05976	-3.15	1.63	0.7963
2457058.08085	-7.34	1.58	0.7784

(This table is available in its entirety in machine-readable form.)

Table 5
GJ3470 Relative RV Measurements

BJD _{TDB}	RV (m s ⁻¹)	Unc. (m s ⁻¹)	S_{HK}	Instrument
2456196.12523	7.28	1.59	0.846	HIRES
2456203.092443	8.42	1.8	0.905	HIRES
2455987.609282	26499.6	5.53	...	HARPS
2455988.600211	26509.13	3.66	...	HARPS

(This table is available in its entirety in machine-readable form.)

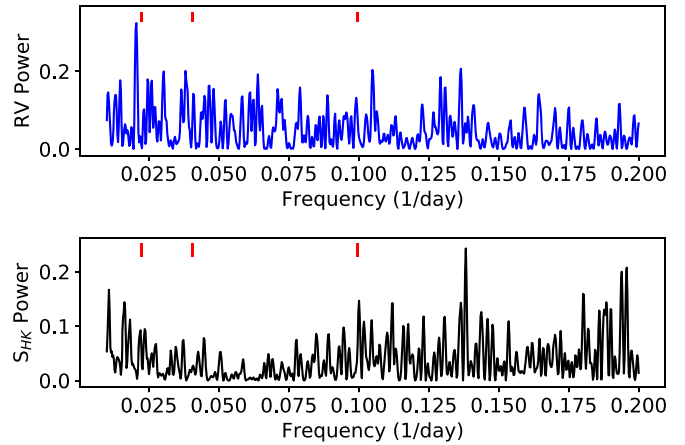


Figure 4. K2-3: periodograms of the RV data (top) and S_{HK} (bottom). The orbital periods of the three planets are shown by red tick marks at the top of the figures. The RV and S_{HK} periodogram do not have similar prominent peaks. Although the planet periods are not all visible in the RV periodogram due to their meter per second RV amplitudes, we are able to detangle the planet signals in the RV data by constraining the periods and conjunction times from K2 and *Spitzer* transits.

Evryscope light curves are generated using a custom pipeline. The Evryscope image archive contains 2.5 million raw images, ~ 250 TB of total data. Each image, consisting of a 30 MPix FITS file from one camera, is dark-subtracted, flat-fielded, and then astrometrically calibrated using a custom wide-field solver. Large-scale background gradients are removed, and forced-aperture photometry is then extracted based on known source positions in a reference catalog. Light curves are generated for approximately 15 million sources across the southern sky by differential photometry in small sky regions using carefully selected reference stars; residual systematics are removed using two iterations of the SysRem detrending algorithm. For 10th mag stars, this process results in $\approx 1\%$ photometric stability at two-minute cadence when measured in multiple-year light curves over all sky conditions; co-adding produces improved precisions, down to ~ 6 mmag.

Evryscope collected 9931 epochs of K2-3 at two-minute cadence in Sloan- g' from 2016 January to 2018 March. The data were analyzed using a Lomb-Scargle (LS) periodogram to determine the likely rotation period of K2-3 (Figure 5). The highest peak is at 40.0 days, but power from the central peak is split due to the inter-year window function, verified by injecting similar signals to K2-3 and other nearby stars. An alias of the 40.0 day signal exists at a reduced power near 20 days. The periodogram for only the 2017 photometry produces a peak signal of 38 days. A signature of evolving starspot activity due to differential rotation near 40 days may explain this difference. The 40.0 day period shows a sinusoidal variation with a 0.02 mag variation. Therefore, we infer the rotation period of K2-3 to be 40 ± 2 days from the Evryscope data. Both the 2017 and the all-data rotation periods agree with the estimate from K2 data, within measurement errors. We use the Evryscope photometry to inform our GP priors in the RV fit (Section 4.3.2).

4.2.2. GJ3470 Stellar Activity

To better characterize GJ3470, photometry was collected at the Fairborn Observatory in Arizona with the Tennessee State University Celestron C14 0.36 m Automated Imaging

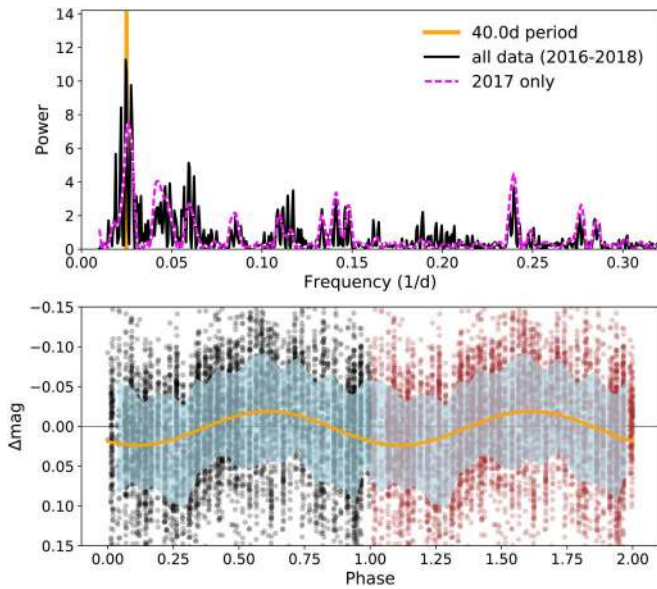


Figure 5. Evryscope photometry of K2-3, consisting of 9931 epochs at two-minute cadence in Sloan- g' from 2016 January to 2018 March. Top panel: the Lomb–Scargle (LS) periodogram of K2-3 displays significant power around 40 days (orange vertical line). A purple dashed line shows the power of only the 2017 photometry as a secondary confirmation. Bottom panel: phase-folded light curve folded over 40 days. The phase is repeated to guide the eye, and points are binned to eight-minute cadence to improve precision on this relatively faint Evryscope target. The 1σ region about the mean of the phased light curve is shown (light blue area), along with a 40-day sinusoid with a characteristic amplitude of 0.02 mag (orange curve).

Telescope (AIT; Henry 1999; Eaton et al. 2003). The AIT has a SBIG STL-1001E CCD camera and a Cousins R filter. Images were corrected for bias, flat-fielding, and differential extinction. Differential magnitudes were computed using five field stars. 842 observations were collected from 2012 December to 2017 May (Figure 6; Table 6).

The tallest peak in the periodogram (Figure 6) corresponds to a period of 21.54 ± 0.49 days; the uncertainty is the standard deviation between the peaks for each observing season. We interpret this peak as the stellar rotation period, as shown by the brightness variation from star spots rotating in and out of view. This rotation period is consistent with that found by Biddle et al. (2014).

For GJ3470, there is a hint of an RV- S_{HK} correlation in the early HIRES data, although the full data set has a correlation coefficient of -0.0753 and p -value of 0.5812. Furthermore, the RV periodogram contains a significant peak near the stellar rotation period (Figure 7), which suggests that the stellar rotation signal needs to be accounted for in the RV analysis. We therefore used this photometry to inform our GP priors in the RV fit (Section 4.3.1).

4.3. RV Analysis

We analyzed the RV data for both systems using RadVel, an open-source orbit-fitting toolkit for RV data (Fulton et al. 2018). RadVel models the RVs as the sum of Keplerian orbits. The model parameters are orbital period (P), time of inferior conjunction (T_{conj}), RV amplitude (K), eccentricity (e), argument of periastron (ω), a constant RV offset (γ), and a jitter term for each instrument (σ). In order to avoid biasing

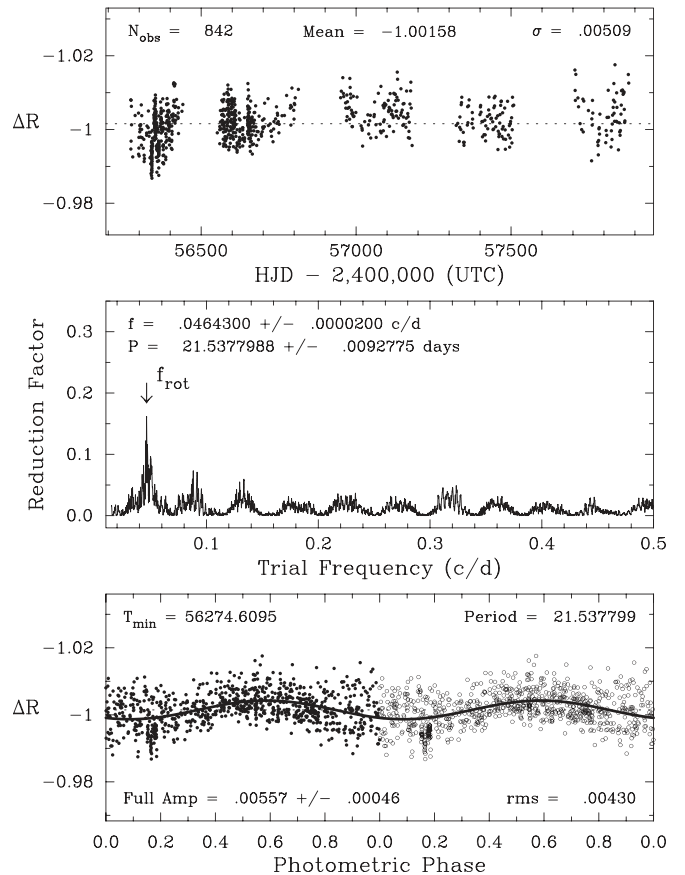


Figure 6. Top: photometry of GJ3470 from 2012 to 2017 from the C14 AIT at Fairborn Observatory. Middle: power spectrum in frequency space resulted in a stellar rotation period of 21.54 days. We inflated the period uncertainty to 21.54 ± 0.49 days, to account for the variation in rotation period over time. Bottom: phased photometry over the periodogram peak at 21.54 days.

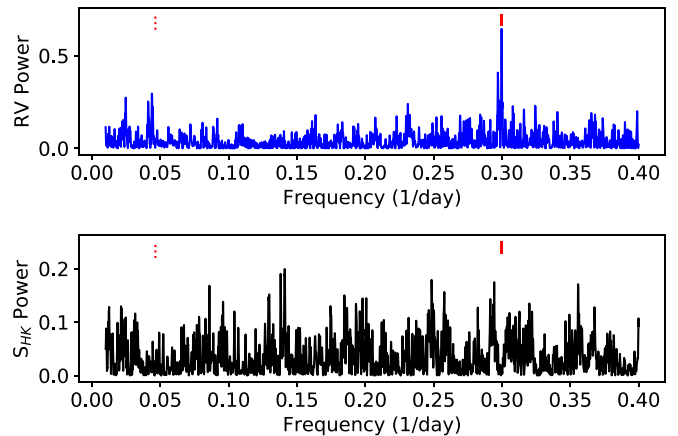


Figure 7. GJ3470: periodogram of the RV data (top) and S_{HK} periodogram (bottom). The main peak in RV at 3.3 days matches the period of planet b (red tick mark). The next prominent peaks are near the stellar rotation period (red dotted mark; see Figure 6). The RV and S_{HK} periodograms do not have any prominent peaks in common.

eccentricity, $\sqrt{e} \cos(\omega)$ and $\sqrt{e} \sin(\omega)$ are used as fitting parameters.

We modeled the correlated noise introduced from the stellar activity using a quasi-periodic GP with a covariance kernel of

Table 6
Summary of C14 AIT Photometric Observations of GJ3470

Observing Season	Date Range (HJD-2400,000)	N_{obs}	Sigma (mag)	Seasonal Mean (mag)
2012–2013	56272–56440	297	0.00535	-0.99917 ± 0.00031
2013–2014	56551–56813	289	0.00397	-1.00205 ± 0.00023
2014–2015	56949–57180	108	0.00419	-1.00494 ± 0.00040
2015–2016	57323–57508	83	0.00384	-1.00214 ± 0.00042
2016–2017	57705–57879	65	0.00586	-1.00417 ± 0.00073

the form

$$k(t, t') = \eta_1^2 \exp \left[-\frac{(t - t')^2}{\eta_2^2} - \frac{\sin^2 \left(\frac{\pi(t - t')}{\eta_3} \right)}{\eta_4^2} \right], \quad (1)$$

where the hyper-parameter η_1 is the amplitude of the covariance function, η_2 is the active region evolutionary timescale, η_3 is the period of the correlated signal, and η_4 is the length scale of the periodic component (Haywood et al. 2014; López-Morales et al. 2016). We trained these parameters on the ground-based photometry of each star by performing a maximum likelihood fit to the associated ground-based light curve with the quasi-periodic kernel (Equation (1)) then determined the errors through a MCMC analysis. We then compare the period of the correlated signal (η_3) with the stellar rotation period found from our periodogram analysis in Section 4.2.

4.3.1. GJ3470 RV Analysis

For our RV analysis of GJ3470, we adopt the period, time of conjunction, and planet radius derived from a variety of ground-based telescopes (Biddle et al. 2014). The remaining parameters were initialized from Dragomir et al. (2015).

We used a GP to model the correlated noise associated with the stellar activity in our RV fit. We ran our GP analysis on the photometry from Fairborn Observatory (FO; Section 4.2) and find $\gamma_{\text{FO}} = 1.003 \pm 0.001$, $\sigma_{\text{FO}} = 0.0029 \pm 0.0001$, $\eta_1 = -0.0036_{-0.0004}^{+0.0003}$, $\eta_2 = 48.98_{-7.28}^{+9.54}$, $\eta_3 = 21.84_{-0.36}^{+0.35}$, and $\eta_4 = 0.55 \pm 0.06$. This stellar rotation period (η_3) is consistent with the results of our periodogram analysis in Section 4.2 to within 1σ .

We then perform our RV fit including a GP modeled as a sum of two quasi-periodic kernels, one for each instrument, as HIRES and HARPS have different properties that could alter the effect of stellar activity on the data. Each kernel includes identical η_2 , η_3 , and η_4 parameters but allows for different η_1 values. Our priors are as follows: η_1 is left as a free parameter as light curve amplitude cannot be directly translated to RV amplitude, for η_2 , η_3 , and η_4 , we used a kernel density estimate (KDE) of the FO photometry posteriors.

After running an initial RV fit including only one circular, Keplerian planet signal, we investigated models including an acceleration term, curvature term, and eccentricity. The Aikike information criterion (AIC) was used to determine if the fit improvement justified the additional parameters; a ΔAIC of <2 indicates a similar fit, $2 < \Delta\text{AIC} < 10$ favors the additional parameter, and a $\Delta\text{AIC} > 10$ is a strong justification for the additional parameter. Only the eccentricity parameters improved the AIC ($\Delta\text{AIC}_{\text{acc}} = -0.71$, $\Delta\text{AIC}_{\text{curv}} = -1.44$,

Table 7
GJ3470 RV MCMC Priors and Posteriors

Parameter	Value	Units
<i>Gaussian Priors</i>		
T_{conj_b}	2455953.6645 ± 0.0034	JD
P_b	3.3371 ± 0.0002	days
$e \cos \omega_b$	0.01454 ± 0.00075323	
$\eta_{1,\text{HIRES}}$	[0, 100]	m s^{-1}
$\eta_{1,\text{HARPS}}$	[0, 100]	m s^{-1}
η_2	$48.98_{-7.28}^{+9.54}$	days
η_3	$21.84_{-0.36}^{+0.35}$	days
η_4	0.55 ± 0.006	...
<i>Orbital Parameters</i>		
P_b	$3.336649_{-8.1e-05}^{+8.4e-05}$	days
T_{conj_b}	2455953.663 ± 0.0035	JD
e_b	$0.114_{-0.051}^{+0.052}$...
ω_b	$-1.44_{-0.04}^{+0.1}$	radians
K_b	$8.21_{-0.46}^{+0.47}$	m s^{-1}
M_b	$12.58_{-1.28}^{+1.31}$	M_{\oplus}
ρ_b	$0.93_{-0.31}^{+0.56}$	g cm^{-3}
<i>Other Parameters</i>		
γ_{HIRES}	$0.3_{-1.1}^{+1.2}$	m s^{-1}
γ_{HARPS}	$26500.52_{-0.6}^{+0.59}$	m s^{-1}
$\dot{\gamma}$	$\equiv 0.0$	$\text{m s}^{-1} \text{ day}^{-1}$
$\ddot{\gamma}$	$\equiv 0.0$	$\text{m s}^{-1} \text{ day}^{-2}$
σ_{HIRES}	$1.9_{-0.67}^{+0.7}$	m s^{-1}
σ_{HARPS}	$0.0023_{-0.0023}^{+0.49}$	m s^{-1}
$\eta_{1,\text{HIRES}}$	$3.94_{-0.78}^{+0.90}$	m s^{-1}
$\eta_{1,\text{HARPS}}$	$1.79_{-0.71}^{+0.69}$	m s^{-1}
η_2	$49.40_{-7.55}^{+10.00}$	days
η_3	$21.92_{-0.41}^{+0.42}$	days
η_4	0.56 ± 0.06	...

and $\Delta\text{AIC}_{\text{ecc}} = 6.45$). All of the tested RV models resulted in planet masses within 1σ of the circular fit values shown in Table 7

We then investigated a model including an eccentricity constraint from *Spitzer* observations of the secondary eclipse. The secondary eclipse was 0.309 days later than expected for a circular orbit, which results in a constraint on $e \cos(\omega)$ of $0.014546_{-0.000659}^{+0.000753}$ (Benneke in review). For this fit we used $e \cos(\omega)$ and $e \sin(\omega)$ as the fitting basis due to the prior set by the secondary eclipse. We find an eccentricity of $e_b = 0.114 \pm 0.051$ for the eccentric model constrained by this secondary eclipse measurement, the best-fit curve is shown in Figure 8.

The non-zero eccentricity value of GJ3470 b is particularly interesting in the context of other systems. GJ436 b, another planet similar in mass, radius, period, and stellar host, has a puzzlingly high eccentricity of 0.150 ± 0.012 (Deming et al. 2007). These high eccentricity values may be an emerging clue on how these types of planets form and migrate.

4.3.2. K2-3 RV Analysis

For our RV analysis of K2-3, we adopt the planet orbital periods and times of conjunction from our *Spitzer* analysis (Section 3). We used a GP to model the correlated noise associated with the stellar activity in our RV fit. We ran our GP analysis on the photometry from Evryscope (ES; Section 4.2) and find $\gamma_{\text{ES}} = 11.61 \pm 0.01$, $\sigma_{\text{ES}} = 0.017_{-0.003}^{+0.004}$, $\eta_1 = 0.03 \pm$

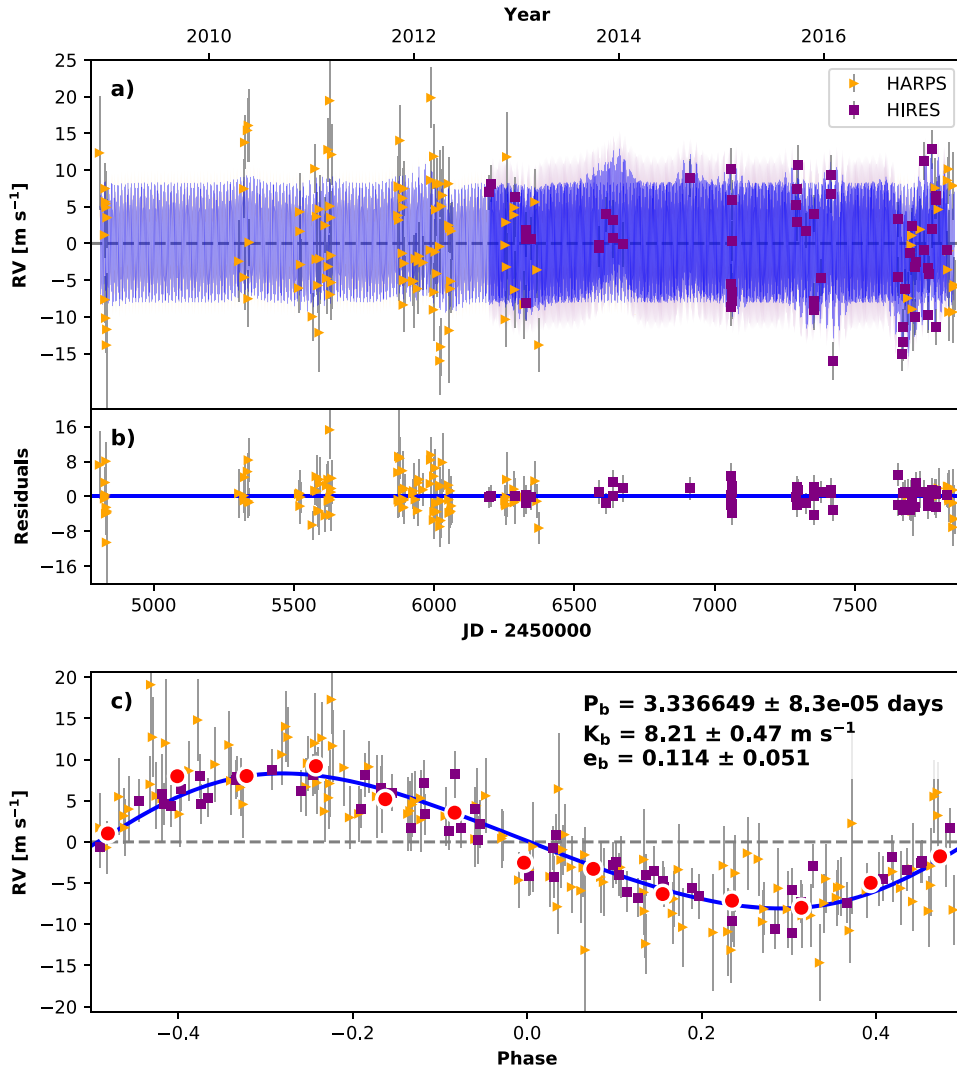


Figure 8. Best-fit one-planet Keplerian orbital model for GJ3470 with $\text{ecos}(\omega)$ constraints from the secondary eclipse observation. The maximum likelihood model is plotted while the orbital parameters listed in Table 7 are the median values of the posterior distributions. The thin blue line is the best-fit one-planet model with the mean GP model and the colored area surrounding this line includes the 1σ maximum likelihood GP uncertainties. We add in quadrature the RV jitter term(s) listed in Table 7 with the measurement uncertainties for all RVs. (b) Residuals to the best-fit one-signal model. (c) RVs phase-folded to the ephemeris of planet b. The small point colors and symbols are the same as in panel (a). The red circles are the same velocities binned in 0.08 units of orbital phase.

0.01, $\eta_2 = 44.57^{+12.58}_{-16.23}$, $\eta_3 = 37.80^{+1.77}_{-2.04}$, and $\eta_4 = 0.47 \pm 0.05$. This stellar rotation period (η_3) is consistent with the results of our periodogram analysis in Section 4.2 to within 2σ .

We then perform our RV fit including a GP modeled as a sum of four quasi-periodic kernels, one for HIRES, HARPS, HARPS-N, and PFS, as described above for GJ3470. Our GP hyper-parameter priors are as follows: η_1 is left as a free parameter as light curve amplitude cannot be directly translated to RV amplitude. To construct priors on η_2 , η_3 , and η_4 , we use a KDE of the Evryscope photometry posteriors.

After running an initial RV fit including only three circular, Keplerian planet signals, we investigated additional models including an acceleration term, curvature term, and planet eccentricity. The fit including an additional term for acceleration, curvature, and eccentricity had ΔAIC of -2.17 , -2.22 , and -2.92 respectively; none of these justified the additional parameter. Table 8 shows the MCMC priors, orbital parameters, and statistics for the GP model of K2-3. The best-fit curves for each planet is shown in Figure 9.

From our GP fit, we find that the semi-amplitude of the signal from planet d is consistent with 0 to 1σ . It is possible that this planet has a small semi-amplitude ($K_d \ll \text{m s}^{-1}$) and we were unable to detect it. Alternatively, as the period of planet d ($P_d = 44.56$ days) is near the stellar rotation period ($\eta_3 \approx 40$ days), it is possible that the signal of planet d is indistinguishable from the stellar activity signal. Further work is needed to distinguish between the two possibilities and determine the mass of planet d.

5. Discussion

These four Earth- to Neptune-sized planets are great candidate targets for atmospheric transmission spectroscopy due to their bright host stars ($K < 9$ mag) and low densities ($< 4.2 \text{ g cm}^{-3}$). GJ3470 b has been observed with the *Hubble Space Telescope* (HST) in cycles 19 and 22 (GO 13064, GO 13665). K2-3 d and the K2-3 UV emission will be observed in cycles 24 and 25 (GO 14682, GO 15110). GJ3470 b already shows H_2O absorption (Tsiaras et al. 2018); Benneke et al.

Table 8
K2-3 RV MCMC Priors and Posteriors

Parameter	Three-planet Fit	Units
<i>Gaussian Priors</i>		
T_{conj_b}	$2456813.41843 \pm 0.00039$	JD
P_b	$10.054626 \pm 1e - 05$	days
T_{conj_c}	$2456812.28013 \pm 0.00095$	JD
P_c	$24.646582 \pm 3.9e - 05$	days
T_{conj_d}	$2456826.22347 \pm 0.00053$	JD
P_d	$44.556456 \pm 9.7e - 05$	days
$\eta_{1,\text{all}}$	[0, 100]	m s^{-1}
η_2	$44.57^{+12.58}_{-16.23}$	days
η_3	$37.80^{+1.77}_{-2.04}$	days
η_4	0.47 ± 0.05	...
<i>Orbital Parameters</i>		
P_b	$10.054626^{+1e-05}_{-1.1e-05}$	days
T_{conj_b}	$2456813.41843 \pm 0.00041$	JD
e_b	$\equiv 0.0$...
ω_b	$\equiv 0.0$	radians
K_b	$2.72^{+0.29}_{-0.3}$	m s^{-1}
M_b	$6.48^{+0.99}_{-0.93}$	M_{\oplus}
ρ_b	$3.70^{+1.67}_{-1.08}$	g cm^{-3}
P_c	$24.646582^{+4.1e-05}_{-4e-05}$	days
T_{conj_c}	$2456812.28018^{+0.00098}_{-0.001}$	JD
e_c	$\equiv 0.0$...
ω_c	$\equiv 0.0$	radians
K_c	0.67 ± 0.32	m s^{-1}
M_c	$2.14^{+1.08}_{-1.04}$	M_{\oplus}
ρ_c	$2.98^{+1.96}_{-1.50}$	g cm^{-3}
P_d	$44.55646^{+0.00011}_{-0.0001}$	days
T_{conj_d}	$2456826.22346 \pm 0.00056$	JD
e_d	$\equiv 0.0$...
ω_d	$\equiv 0.0$	radians
K_d	$-0.13^{+0.28}_{-0.31}$	m s^{-1}
M_d	$-0.50^{+1.10}_{-1.20}$	M_{\oplus}
ρ_d	$-0.98^{+2.20}_{-2.83}$	g cm^{-3}
K_d (3σ upper)	0.71	m s^{-1}
M_d (3σ upper)	2.80	M_{\oplus}
ρ_d (3σ upper)	5.62	g cm^{-3}
<i>Other Parameters</i>		
γ_{PFS}	-1.3 ± 2.2	m s^{-1}
γ_{HIRES}	$-2.98^{+0.97}_{-1.0}$	m s^{-1}
$\gamma_{\text{HARPS-N}}$	$0.53^{+0.71}_{-0.74}$	m s^{-1}
γ_{HARPS}	$-0.59^{+0.69}_{-0.73}$	m s^{-1}
$\dot{\gamma}$	$\equiv 0.0$	$\text{m s}^{-1} \text{ day}^{-1}$
$\ddot{\gamma}$	$\equiv 0.0$	$\text{m s}^{-1} \text{ day}^{-2}$
σ_{PFS}	$4.85^{+1.0}_{-0.88}$	m s^{-1}
σ_{HIRES}	$2.98^{+0.47}_{-0.42}$	m s^{-1}
$\sigma_{\text{HARPS-N}}$	$1.61^{+0.26}_{-0.25}$	m s^{-1}
σ_{HARPS}	$2.06^{+0.34}_{-0.32}$	m s^{-1}
$\eta_{1,\text{PFS}}$	$4.75^{+3.72}_{-2.58}$	m s^{-1}
$\eta_{1,\text{HIRES}}$	$3.21^{+0.84}_{-0.73}$	m s^{-1}
$\eta_{1,\text{HARPS}}$	$3.04^{+0.64}_{-0.53}$	m s^{-1}
$\eta_{1,\text{HARPS-N}}$	$3.07^{+0.61}_{-0.48}$	m s^{-1}
η_2	$62.25^{+10.78}_{-9.84}$	days
η_3	$39.16^{+0.88}_{-0.96}$	days
η_4	$0.41^{+0.05}_{-0.04}$...

2018, submitted) and is being targeted by *JWST* Guaranteed Time Observation (GTO) program observations.

It is important to characterize potential targets to determine precise mass and surface gravity measurements, as these parameters will affect the interpretation of future transmission spectroscopy observations. We examined the potential atmospheric composition of these planets in two ways. First, we investigate their potential compositions in a mass–radius diagram (Figure 10). Fulton et al. (2017) describes a bimodality in occurrence rates of small planets in terms of planet radius with a gap between 1.5 and $2.0 R_{\oplus}$. This distribution in radius suggests a similar distribution in planet composition, where planets smaller than $1.5 R_{\oplus}$ are super-Earths and planets $2.0\text{--}3.0 R_{\oplus}$ are sub-Neptunes. The three K2-3 planets fall in three different places relative to the radius gap (Fulton et al. 2017): planet b lies above, planet c is within the gap, and planet d is just below.

We examine the bulk composition of these four planets in the context of other super-Earth and sub-Neptune planets (Figure 10). GJ3470 b occupies the same mass–radius space as our own ice giants, Uranus and Neptune, and likely also has a substantial volatile envelope. Depending on its core composition, GJ3470 b has between 4% and 13% H/He (Lopez & Fortney 2014). K2-3 b and c both have a bulk density consistent with a mixture of silicates and water. As a water planet is an unlikely product of planet formation, they likely have iron-silicate cores with a small volatile envelope. Assuming an Earth-like core, K2-3 b and c both have about 0.5% H/He by mass (Lopez & Fortney 2014). However, K2-3 c is also consistent with no volatile atmosphere given a sufficient amount of lighter material in the core, and the 3σ mass measurement is consistent with an Earth-like composition. K2-3 d is potentially the lightest planet compared to others of similar radii; it needs substantial volatiles to explain its placement on the mass–radius diagram. The two main interpretations are: (1) the planet is sufficiently of low mass to not detect its signal, requiring a significant volatile percentage, or (2) we have not adequately accounted for the stellar activity RV signal in this analysis, therefore, the actual mass of planet d is higher than listed here.

Our mass measurements of K2-3 b and c are within 1σ of Almenara et al. (2015) and Dai et al. (2016). Our mass measurement of K2-3 d is within 3σ of Dai et al. (2016) and 4σ of Almenara et al. (2015). Our measurements of K2-3 b is within 1σ of Damasso et al. (2018), K2-3 c is within 2σ , and K2-3 d is within 2σ of their RV fit and within 3σ of their injection/recovery tests. We have improved the precision of the mass measurement of all three planets compared to previous measurements, however, due to the potential stellar activity contamination, use caution with the measurement for K2-3 d.

We then simulated model transmission spectra for the K2-3 planet system using ExoTransmit (Kempton et al. 2017) to examine their possible atmospheric compositions (Figure 11). Two spectra were created for planet b and c according to the 1σ lower and upper bounds on the mass. Two spectra were created for planet d according to the upper 2σ and upper 3σ mass, as the mass measurement is consistent with zero. Our assumptions include no clouds, chemical equilibrium, a 100 M/H ratio, and the 1 bar radius equals the transit radius.

The transit depth was adjusted to match the *K2* (Crossfield et al. 2015) and *Spitzer* transit depths. Simulated *JWST*

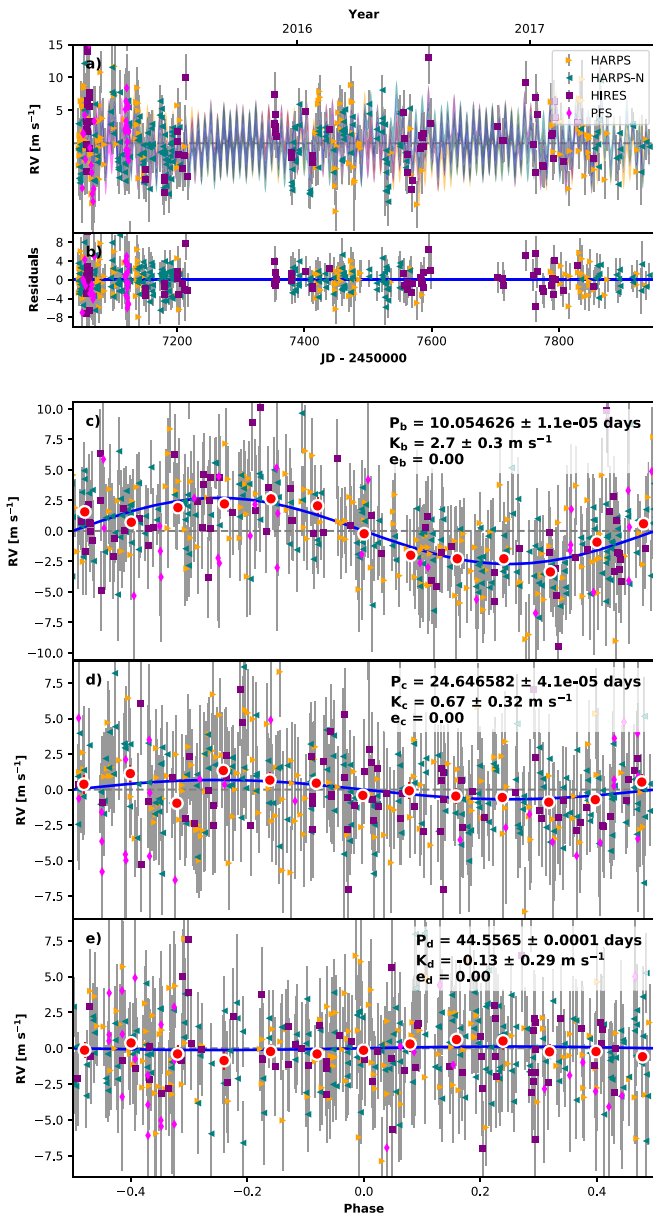


Figure 9. Best-fit three-planet Keplerian orbital model for K2-3. The maximum likelihood model is plotted while the orbital parameters listed in Table 8 are the median values of the posterior distributions. The thin blue line is the best-fit three-planet model with the mean GP model. The colored area surrounding this line includes the 1σ maximum likelihood GP uncertainties. We add in quadrature the RV jitter term(s) listed in Table 8 with the measurement uncertainties for all RVs. (b) Residuals to the best-fit three-planet model. (c) RVs phase-folded to the ephemeris of planet b. The Keplerian orbital models for all other planets have been subtracted. The small point colors and symbols are the same as in panel (a). The red circles are the same velocities binned in 0.08 units of orbital phase. The phase-folded model for planet b is shown as the blue line. Panel (d) and (e) are the same as panel (c) but for planet K2-3 c and d, respectively.

observations and error bars are superimposed on top of the spectra using PandExo³³ (Greene et al. 2016; Batalha et al. 2017b). We simulated one transit for each planet with three instrument modes: NIRCcam F332W2, NIRCcam F444W, and NIRISS SOSS_Or1. We used the Phoenix grid models to simulate a stellar spectrum with a magnitude of 8.56 K mag,

³³ We present a wrapper for easier PandExo simulations, available at <https://github.com/iancrossfield/jwstprep>.

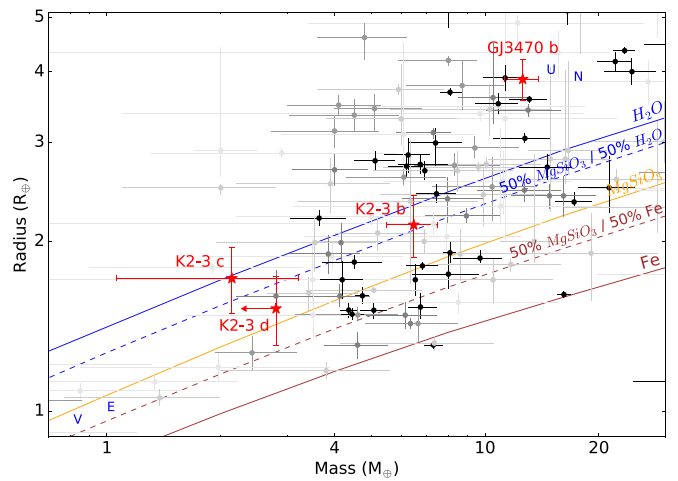


Figure 10. Mass-radius diagram for planets between the size of Earth and Neptune (darker points for smaller error). The compositional curves listed are theoretical models (Zeng et al. 2016) for planets with an iron (brown), silicate (orange), and water (blue) composition. K2-3 b, c, and GJ3470 b (red stars) are shown with 1σ uncertainties along with the K2-3 d 3σ upper limit on mass. All four planets likely have volatile-rich envelopes.

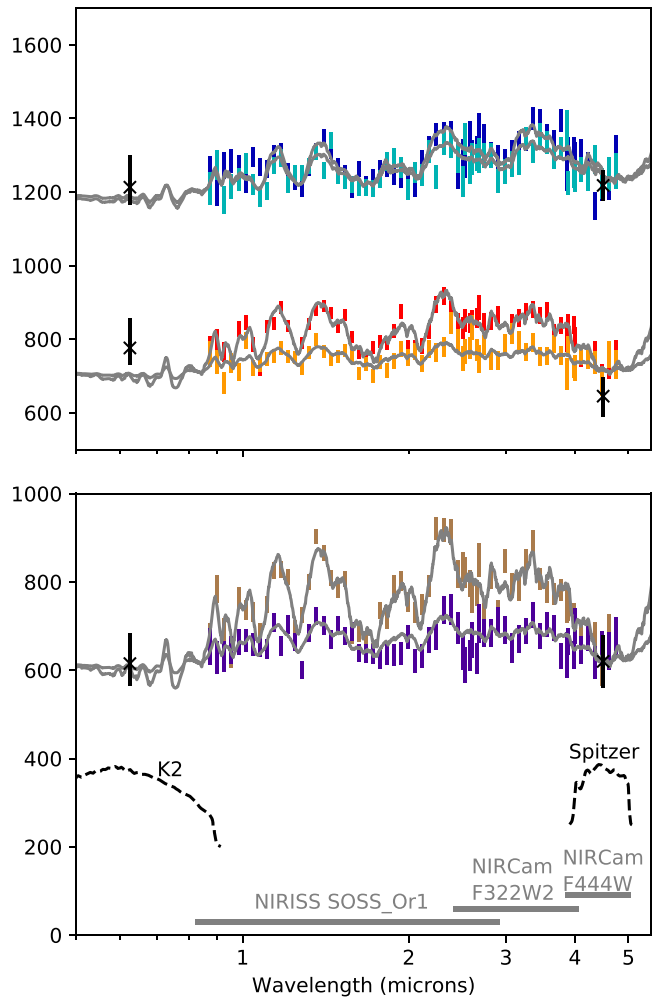


Figure 11. (ppm) Simulated transmission spectra (gray) of K2-3 b (blue/green, top) and c (red/orange, middle) for their 1σ low-mass and high-mass cases and spectra for K2-3 d (brown/purple, bottom) for the upper 1σ and 2σ cases. The error bars refer to simulated JWST observations with PandExo (Batalha et al. 2017b). K2 and Spitzer data points and bandpasses are shown in black. The JWST instrument wavelength ranges are shown in gray. Note the break in the y-axis used for clarity.

temperature of 3890 K, metallicity of 0.3, and $\log(g)$ of 4.8. For each transit, we included a baseline of equal time to the transit time, zero noise floor, and resolution of $R = 35$.

For K2-3 b, the absorption features would be observable for a true mass value within 1σ of our mass measurement; the light and dark blue simulated data points are both inconsistent with a flat spectra. From this, K2-3 b is particularly a good target for future atmospheric study. For K2-3 c, the absorption features would be easily observable for a mass on the lower 1σ side of our measurement, but would be much more difficult for the higher mass case. Lastly, K2-3 d would have distinguishable features as long as the mass is lower than our 2σ upper limit.

The *Spitzer* transit depths for K2-3 c and d are quite similar (Figure 2) although their *K2* transit depths are considerably offset. Beichman et al. (2016) also find similar *Spitzer* transit depths for K2-3 c and d. We were unable to create a model spectra for planet c that was consistent with both the *K2* and *Spitzer* data to 1σ . However, this model did not include clouds, which could improve the fit of the model to the data (Sing et al. 2016).

Transmission spectra can help to constrain a planet’s mass further as the scale height depends on the planet’s gravity (de Wit & Seager 2013). However, one must be careful as there are significant degeneracies between the effects of mass and composition for small planets (Batalha et al. 2017a). With the mass of the planets constrained here through the RV method, further constraints can be put on the atmospheric composition from the transmission spectra.

These planets are example training cases for future TESS planets. TESS will find a large sample of bright systems around nearby stars (Ricker et al. 2014; Sullivan et al. 2015; Ballard 2018). These types of planets will be ideal for *JWST* atmospheric observations due to their bright host stars. Prior to transmission spectroscopy observations, these systems will need to be followed up in a similar method as described in this paper to determine the planet masses in order to correctly interpret the spectra.

6. Conclusion

In summary, we report improved masses, radii, and densities for four planets in two systems, K2-3 and GJ3470, derived from a combination of new RV, photometry, and transit observations. Our primary results are as follows.

Transit follow-ups are key for refining planet ephemerides sufficiently for future characterization. Extending the observation baseline with *Spitzer* greatly narrows the projected transit window. Our uncertainties are 20 times smaller than the original *K2* data, which decreases the 3σ uncertainty in the *JWST* era for planet d from ~ 25 hr to under 30 minutes (Figure 3). Our additional *Spitzer* data improve the ephemeris for the K2-3 planets to one-thirds that of Beichman et al. (2016). See Section 3 for our *Spitzer* analysis and discussion.

S_{HK} may not be a good indicator for stellar activity in M dwarfs. For GJ3470, there was little to no correlation between the RVs and S_{HK} , however, the rotation period found by our photometric monitoring was present in our RV data. For K2-3, although there was no correlation with S_{HK} , our Evryscope photometry showed clear periodicity near the orbital period of K2-3d. Photometry and $H\alpha$ can be useful diagnostics for M-dwarf stellar rotation periods instead of S_{HK} (Robertson et al. 2015; Newton et al. 2017; Damasso et al. 2018). See Sections 4.2.1 and 4.2.2 for a description of our S_{HK} values and stellar activity discussion.

Photometric monitoring of planet-hosting stars is important to determine the stellar rotation period and spot modulation to therefore separate the stellar activity from the planet-induced RV signals. This is especially important for planetary systems with low-amplitude RV signals as these signals may be hidden by stellar activity. We used a GP trained on our photometry to increase the accuracy of our RV fits. See Section 4.3 for our RV analysis including this GP.

From our radial velocity analysis, we determine the mass of GJ3470 b to nearly 10σ ($M_b = 12.58^{+1.31}_{-1.28} M_{\oplus}$), see Section 4.3.2. We additionally constrain the planet eccentricity ($e_b = 0.114^{+0.52}_{-0.51} M_{\oplus}$) from our RV analysis and a measured secondary eclipse from *Spitzer*. Non-zero eccentricities may be an emerging clue on how warm-Neptunes form and migrate.

We have determined an upper limit on the mass of K2-3 d of $2.80 M_{\oplus}$. With such a low mass, this planet is consistent with having a substantial volatile envelope which decreases its chance for habitability. As such, K2-3 likely hosts three sub-Neptune planets instead of super-Earth planets. These planets present an interesting case for transmission spectroscopy observations of temperate sub-Neptunes. See Section 5 for simulated transmission spectra of these three planets.






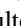



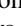



M.R.K. acknowledges support from the NSF Graduate Research Fellowship, grant No. DGE 1339067. I.J.M.C. acknowledges support from NASA through K2GO grant 80NSSC18K0308 and from NSF through grant AST-1824644. G.W.H. acknowledges long-term support from NASA, NSF, Tennessee State University, and the State of Tennessee through its Centers of Excellence program. O.F. acknowledges funding support by the grant MDM-2014-0369 of the ICCUB (Unidad de Excelencia “María de Maeztu”). This work is based [in part] on observations made with the *Spitzer Space Telescope*, which is operated by the Jet Propulsion Laboratory, California Institute of Technology under a contract with NASA. This research has made use of the Exoplanet Follow-up Observing Program (ExoFOP), which is operated by the California Institute of Technology, under contract with the National Aeronautics and Space Administration.




The authors wish to recognize and acknowledge the very significant cultural role and reverence that the summit of Maunakea has always had within the indigenous Hawaiian community. We are most fortunate to have the opportunity to conduct observations from this mountain.

Facilities: Keck:I, *Spitzer*, TNG.

ORCID iDs

Molly R. Kosiarek  <https://orcid.org/0000-0002-6115-4359>
Kevin K. Hardegree-Ullman  <https://orcid.org/0000-0003-3702-0382>

John H. Livingston  <https://orcid.org/0000-0002-4881-3620>
Gregory W. Henry  <https://orcid.org/0000-0003-4155-8513>
Ward S. Howard  <https://orcid.org/0000-0002-0583-0949>
David Berardo  <https://orcid.org/0000-0001-6298-412X>
Sarah Blunt  <https://orcid.org/0000-0002-3199-2888>
Benjamin J. Fulton  <https://orcid.org/0000-0003-3504-5316>
Lea A. Hirsch  <https://orcid.org/0000-0001-8058-7443>
Andrew W. Howard  <https://orcid.org/0000-0001-8638-0320>
Howard Isaacson  <https://orcid.org/0000-0002-0531-1073>
Erik A. Petigura  <https://orcid.org/0000-0003-0967-2893>
Evan Sinukoff  <https://orcid.org/0000-0002-5658-0601>
Lauren Weiss  <https://orcid.org/0000-0002-3725-3058>
Courtney D. Dressing  <https://orcid.org/0000-0001-8189-0233>

Joshua E. Schlieder  <https://orcid.org/0000-0001-5347-7062>
 Farisa Y. Morales  <https://orcid.org/0000-0001-9414-3851>
 Nicholas M. Law  <https://orcid.org/0000-0001-9380-6457>

References

- Almenara, J. M., Astudillo-Defru, N., Bonfils, X., et al. 2015, *A&A*, **581**, L7
 Astudillo-Defru, N., Bonfils, X., Delfosse, X., et al. 2015, *A&A*, **575**, A119
 Astudillo-Defru, N., Forveille, T., Bonfils, X., et al. 2017, *A&A*, **602**, A88
 Ballard, S. 2018, arXiv:1801.04949
 Batalha, N. E., Kempton, E. M.-R., & Mbarek, R. 2017a, *ApJL*, **836**, L5
 Batalha, N. E., Mandell, A., Pontoppidan, K., et al. 2017b, *PASP*, **129**, 064501
 Beichman, C., Livingston, J., Werner, M., et al. 2016, *ApJ*, **822**, 39
 Benneke, B., Werner, M., Petigura, E., et al. 2017, *ApJ*, **834**, 187
 Biddle, L. I., Pearson, K. A., Crossfield, I. J. M., et al. 2014, *MNRAS*, **443**, 1810
 Bodenheimer, P., & Lissauer, J. J. 2014, *ApJ*, **791**, 103
 Bonfils, X., Gillon, M., Udry, S., et al. 2012, *A&A*, **546**, A27
 Bourrier, V., Lecavelier des Etangs, A., Ehrenreich, D., et al. 2018, *A&A*, **620**, A147
 Bradley, L., Sipocz, B., Robitaille, T., et al. 2016, *astropy/photutils: v0.3*, Zenodo, doi:10.5281/zenodo.164986
 Buccino, A. P., Díaz, R. F., Luoni, M. L., Abrevaya, X. C., & Mauas, P. J. D. 2011, *AJ*, **141**, 34
 Chen, G., Guenther, E. W., Pallé, E., et al. 2017, *A&A*, **600**, A138
 Cincunegui, C., Díaz, R. F., & Mauas, P. J. D. 2007, *A&A*, **469**, 309
 Claret, A., & Bloemen, S. 2011, *A&A*, **529**, A75
 Claret, A., Hauschildt, P. H., & Witte, S. 2012, *yCat*, **354**
 Crossfield, I. J. M., Barman, T., Hansen, B. M. S., & Howard, A. W. 2013, *A&A*, **559**, A33
 Crossfield, I. J. M., Ciardi, D. R., Petigura, E. A., et al. 2016, *ApJS*, **226**, 7
 Crossfield, I. J. M., Petigura, E., Schlieder, J. E., et al. 2015, *ApJ*, **804**, 10
 Cutri, R. M., Skrutskie, M. F., van Dyk, S., et al. 2003, *yCat*, **2246**
 Dai, F., Winn, J. N., Albrecht, S., et al. 2016, *ApJ*, **823**, 115
 Damasso, M., Bonomo, A. S., Astudillo-Defru, N., et al. 2018, *A&A*, **615**, A69
 de Wit, J., & Seager, S. 2013, *Sci*, **342**, 1473
 Deming, D., Harrington, J., Laughlin, G., et al. 2007, *ApJL*, **667**, L199
 Deming, D., Knutson, H., Kammer, J., et al. 2015, *ApJ*, **805**, 132
 Demory, B.-O., Torres, G., Neves, V., et al. 2013, *ApJ*, **768**, 154
 Dragomir, D., Benneke, B., Pearson, K. A., et al. 2015, *ApJ*, **814**, 102
 Dressing, C. D., & Charbonneau, D. 2013, *ApJ*, **767**, 95
 Dressing, C. D., & Charbonneau, D. 2015, *ApJ*, **807**, 45
 Dressing, C. D., Vanderburg, A., Schlieder, J. E., et al. 2017, *AJ*, **154**, 207
 Eaton, J. A., Henry, G. W., & Fekel, F. C. 2003, in *Astrophysics and SpaceScience Library*, Vol. 288, *The Future of Small Telescopes in the NewMillennium: Volume II—The Telescope We Use*, ed. T. D. Oswalt, (Dordrecht: Kluwer), **189**
 Foreman-Mackey, D., Hogg, D. W., Lang, D., & Goodman, J. 2013, *PASP*, **125**, 306
 Fressin, F., Torres, G., Charbonneau, D., et al. 2013, *ApJ*, **766**, 81
 Fukui, A., Livingston, J., Narita, N., et al. 2016, *AJ*, **152**, 171
 Fukui, A., Narita, N., Kurosaki, K., et al. 2013, *ApJ*, **770**, 95
 Fulton, B. J., Petigura, E. A., Blunt, S., & Sinukoff, E. 2018, *PASP*, **130**, 044504
 Fulton, B. J., Petigura, E. A., Howard, A. W., et al. 2017, *AJ*, **154**, 109
 Gomes da Silva, J., Santos, N. C., Bonfils, X., et al. 2012, *A&A*, **541**, A9
 Goodman, J., & Weare, J. 2010, *CAMCS*, **5**, 65
 Greene, T. P., Line, M. R., Montero, C., et al. 2016, *ApJ*, **817**, 17
 Hayashi, C. 1981, *PTHPs*, **70**, 35
 Haywood, R. D., Collier Cameron, A., Queloz, D., et al. 2014, *MNRAS*, **443**, 2517
 Henry, G. W. 1999, *PASP*, **111**, 845
 Howard, A. W., Johnson, J. A., Marcy, G. W., et al. 2010, *ApJ*, **721**, 1467
 Howard, A. W., Marcy, G. W., Bryson, S. T., et al. 2012, *ApJS*, **201**, 15
 Huber, D., Bryson, S. T., Haas, M. R., et al. 2016, *ApJS*, **224**, 2
 Ingalls, J. G., Krick, J. E., Carey, S. J., et al. 2016, *AJ*, **152**, 44
 Isaacson, H., & Fischer, D. 2010, *ApJ*, **725**, 875
 Jones, E., Oliphant, T., & Peterson, P. 2001, *SciPy: Open Source Scientific Tools for Python*, <http://www.scipy.org/>
 Kempton, E. M.-R., Lupu, R., Owusu-Asare, A., Slough, P., & Cale, B. 2017, *PASP*, **129**, 044402
 Kipping, D. M. 2013, *MNRAS*, **435**, 2152
 Knutson, H. A., Lewis, N., Fortney, J. J., et al. 2012, *ApJ*, **754**, 22
 Kreidberg, L. 2015, *PASP*, **127**, 1161
 Law, N. M., Fors, O., Ratzloff, J., et al. 2015, *PASP*, **127**, 234
 Lee, E. J., & Chiang, E. 2016, *ApJ*, **817**, 90
 Lee, E. J., Chiang, E., & Ormel, C. W. 2014, *ApJ*, **797**, 95
 Livingston, J. H., Crossfield, I. J. M., Werner, M. W., et al. 2019, arXiv:1901.05855
 Lopez, E. D., & Fortney, J. J. 2014, *ApJ*, **792**, 1
 López-Morales, M., Haywood, R. D., Coughlin, J. L., et al. 2016, *AJ*, **152**, 204
 Mayo, A. W., Vanderburg, A., Latham, D. W., et al. 2018, *AJ*, **155**, 136
 McQuillan, A., Aigrain, S., & Mazeh, T. 2013, *MNRAS*, **432**, 1203
 Mizuno, H. 1980, *PTHP*, **64**, 544
 Montet, B. T., Morton, T. D., Foreman-Mackey, D., et al. 2015, *ApJ*, **809**, 25
 Mulders, G. D., Pascucci, I., & Apai, D. 2015, *ApJ*, **798**, 112
 Nascimbeni, V., Piotto, G., Pagano, I., et al. 2013, *A&A*, **559**, A32
 Newton, E. R., Irwin, J., Charbonneau, D., et al. 2017, *ApJ*, **834**, 85
 Newton, E. R., Irwin, J., Charbonneau, D., Berta-Thompson, Z. K., & Dittmann, J. A. 2016, *ApJL*, **821**, L19
 Ormel, C. W., Liu, B., & Schoonenberg, D. 2017, *A&A*, **604**, A1
 Petigura, E. A., Howard, A. W., & Marcy, G. W. 2013, *PNAS*, **110**, 19273
 Reid, I. N., Hawley, S. L., & Gizis, J. E. 1997, *yCat*, **3198**
 Ricker, G. R., Winn, J. N., Vanderspek, R., et al. 2014, *Proc. SPIE*, **9143**, 914320
 Robertson, P., Endl, M., Cochran, W. D., & Dodson-Robinson, S. E. 2013, *ApJ*, **764**, 3
 Robertson, P., Endl, M., Henry, G. W., et al. 2015, *ApJ*, **801**, 79
 Rogers, L. A. 2015, *ApJ*, **801**, 41
 Sing, D. K., Fortney, J. J., Nikolov, N., et al. 2016, *Natur*, **529**, 59
 Sullivan, P. W., Winn, J. N., Berta-Thompson, Z. K., et al. 2015, *ApJ*, **809**, 77
 Swift, J. J., Johnson, J. A., Morton, T. D., et al. 2013, *ApJ*, **764**, 105
 Tsiaras, A., Waldmann, I. P., Zingales, T., et al. 2018, *AJ*, **155**, 156
 Van Eylen, V., Agentoft, C., Lundkvist, M. S., et al. 2018, *MNRAS*, **479**, 4786
 Vanderburg, A., Latham, D. W., Buchhave, L. A., et al. 2016, *ApJS*, **222**, 14
 Vogt, S. S., Allen, S. L., Bigelow, B. C., et al. 1994, *Proc. SPIE*, **2198**, 362
 Weidenschilling, S. J. 1977, *Ap&SS*, **51**, 153
 Weiss, L. M., & Marcy, G. W. 2014, *ApJL*, **783**, L6
 Zeng, L., Sasselov, D. D., & Jacobsen, S. B. 2016, *ApJ*, **819**, 127